Phosphate-Tolerant Oxygen Reduction Catalysts
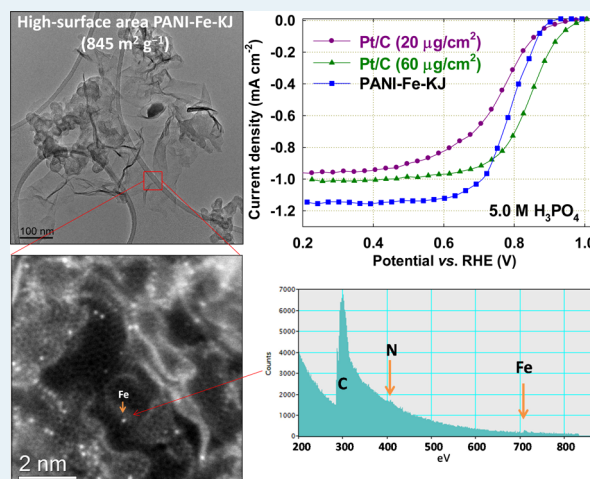
Qing Li,[†] Gang Wu,*,[†] David A. Cullen,[‡] Karren L. More,[#] Nathan H. Mack,[§] Hoon T. Chung,[†] and Piotr Zelenay*,[†]

[†]Materials Physics and Applications Division and [§]Chemistry Division, Los Alamos National Laboratory, Los Alamos, New Mexico 87545, United States

[‡]Materials Science and Technology Division and [#]Center for Nanophase Materials Sciences, Oak Ridge National Laboratory, Oak Ridge, Tennessee 37831, United States

ABSTRACT: Increased oxygen reduction reaction (ORR) kinetics, improved CO tolerance, and more efficient water and heat management represent significant advantages that high-temperature polymer electrolyte fuel cells (HT-PEFCs) operating with a phosphoric acid-doped polybenzimidazole (PBI) membrane offer over traditional Nafion-based, low-temperature PEFCs. However, before such HT-PEFCs become viable, the detrimental effect of phosphate chemisorption on the performance of state-of-the-art Pt-based cathode catalysts needs to be addressed. In this study, we propose a solution to the severe poisoning of Pt-based PEFC cathode catalysts with phosphates ($H_2PO_4^-$ and HPO_4^{2-}) by replacing standard Pt/C catalysts with phosphate-tolerant, nonprecious metal catalyst (NPMC) formulations. Catalysts with a very high surface area ($845 \ m^2 \ g^{-1}$) were synthesized in this work from polyaniline (PANI), iron, and carbon using a high-temperature approach. The effects of metal precursors and metal loading on the morphology, structure, and ORR activity of the NPMCs were systematically studied. Electrochemical measurements indicated that as-prepared Fe-based catalysts (PANI-Fe-C) can tolerate phosphate ions at high concentrations and deliver ORR performance in 5.0 M H_3PO_4 that is superior to that of Pt/C catalysts. A 30 wt % Fe-derived catalyst was found to have the most porous morphology and the highest surface area among studied Fe-based catalysts, which correlates with the highest ORR activity of that catalyst. These cost-effective and well-performing ORR catalysts can potentially replace Pt/C catalysts in phosphoric acid-based HT-PEFCs.

KEYWORDS: oxygen reduction, nonprecious metal catalysis, phosphate tolerance, Pt poisoning, phosphoric acid fuel cells

1. INTRODUCTION

Among the various fuel cell technologies under development today, the high-temperature polymer electrolyte fuel cell (HT-PEFC), operating with a polybenzimidazole (PBI) membrane in the presence of polyphosphoric acid, offers several potential advantages over fuel cells that utilize proton-conducting, low-temperature Nafion membranes.[1] Performance losses due to water flooding in the cathode are a key issue in traditional low-temperature fuel cells. In that context, the operating temperature of a PBI-based HT-PEFC is typically between 150 and 200 °C,[2] preventing the formation of liquid water in the cathode. In addition, hydrogen produced from reformed hydrocarbons is contaminated with low levels of carbon monoxide (CO), which negatively impacts fuel cell performance by poisoning the Pt catalysts. The poisoning effect strongly depends on temperature and becomes much less pronounced at elevated temperatures. Li et al.[3] reported that above 185 °C, phosphoric acid fuel cells (PAFCs) can tolerate up to 3% CO, i.e., carbon monoxide levels present in hydrogen

from reforming of hydrocarbons, thus eliminating the need for subsequent CO removal.

PEFCs operating with Nafion or other perfluorosulfonic-acid membranes rely on liquid water for proton conductivity. This limits their operating temperature to ca. 100 °C, above which such membranes dehydrate and their conductivity drops sharply.[4] H_3PO_4-doped PBI membranes can operate at temperatures above 160 °C and without the need for humidification, reaching a protonic conductivity similar to that of Nafion at 80 °C and 95% relative humidity.[5,6] Other potential benefits of H_3PO_4-doped PBI fuel cells include enhanced kinetics of both electrode reactions at elevated temperatures, the ease of stack assembly with phosphoric acid-saturated polymer membranes, and release of high-quality heat.[7]

The state-of-the-art cathode catalysts for HT-PEFCs are presently based on Pt. However, the oxygen reduction reaction (ORR) activity of Pt-based cathodes is significantly impaired in the presence of H_3PO_4 due to the severe Pt catalyst poisoning by chemisorbed dihydrogen phosphate ($H_2PO_4^-$) and hydrogen phosphate (HPO_4^{2-}) ions.[8−10] One possible way of dealing with cathode poisoning by phosphate ions is to replace the Pt catalyst with nonprecious metal catalysts (NPMCs)[11−19] that, in addition to the obvious cost advantage, can offer improved tolerance to surface-active phosphates. It is worth noting that the large thickness of NPMC-type fuel cell electrodes, up to ca. 100 μm,[20,21] makes them prone to water flooding, negatively impacting cell performance.[22] In a liquid-water-free environment this problem is expected to be largely nonexistent, making NPMCs especially suitable for HT-PEFC applications. Finally, the most active NPMCs today contain ca. 90% carbon, which is susceptible to corrosion at high potentials of the cathode via a reaction with water: $C + 2H_2O \rightarrow CO_2 + 4H^+ + 4e^-$ ($E° = 0.207$ V).[23] The liquid-water-free environment is expected to help the overall durability of NPMCs by significantly lowering water activity. To date, the ORR on NPMCs in phosphoric acid media has been largely unexplored, particularly in terms of the ORR mechanism and synthesis−structure−activity correlations in such media.

The effect of metal precursors and metal loading on the ORR activity and durability of polyaniline (PANI)-derived Fe-based NPMCs are systematically discussed below. To the best of our knowledge, this is the first comprehensive report on the implementation of NPMCs as ORR catalysts in phosphoric acid electrolytes.

2. EXPERIMENTAL SECTION

2.1. Catalyst Synthesis. Ketjenblack EC 300J (KJ-300J) was used as the carbon support in the catalyst synthesis. It was first treated in HCl solution for 24 h to remove metal impurities, followed by a HNO_3 treatment to introduce oxygen-containing functionalities onto the carbon surfaces. In a typical approach,[17,24−26] 2.0 mL of aniline was then dispersed in a 1.0 M HCl solution. The suspension was kept below 10 °C, while 5.0 g of oxidant (ammonium peroxydisulfate, APS) and metal precursors (0.7, 2.3, 9.1 g of $FeCl_3$ or 15.8 g of $Co(NO_3)_2 \cdot 6H_2O$) were added. Then 0.4 g of the acid-treated carbon support was mixed with the above PANI suspension. After constant mixing for 24 h to allow aniline to polymerize, get uniformly mixed, and cover the carbon support, the suspension containing carbon, polymer, and transition metal(s) was vacuum-dried using a rotary evaporator. The ensuing mixture was then heat-treated at 900 °C in an inert nitrogen atmosphere for 1 h. The heat-treated sample was preleached in 0.5 M H_2SO_4 at 80 °C for 8 h to remove unstable and inactive species from the catalyst, followed by a thorough wash with deionized water. Finally, the catalyst was heat-treated again at 900 °C in nitrogen for 3 h. The final product was labeled as PANI-M-C (M: Fe or Co, C: KJ). In order to explore the role of nitrogen and transition metals in the ORR catalysis, the PANI-coated carbon, denoted as PANI-C, was subject to the same heating and chemical post-treatments in a controlled experiment.

2.2. Electrochemical Characterization. The ORR activity and four-electron selectivity in the presence of H_3PO_4 were evaluated using rotating ring electrode (RDE) and rotating ring-disk electrode (RRDE). The electrochemical tests were carried out using a CHI Electrochemical Station (Model 750b)

in a conventional three-electrode cell at a room temperature. A graphite rod and an Ag/AgCl electrode in 3.0 M NaCl were used as the counter and reference electrodes, respectively. The catalyst loading was 0.6 mg cm^{-2}. Performance of the reference Pt catalyst was evaluated using a 20 wt % E-TEK Pt/C catalyst at two loadings: 20 and 60 μg_{Pt} cm^{-2}. The steady-state ORR polarization plots were recorded in an O_2-saturated electrolyte using a potential step of 0.03 V and wait-period of 30 s at each RDE potential. The disk rotation rate was varied between 400 to 2500 rpm. The effect of phosphates on ORR activity was measured in a 0.1 M $HClO_4$ solution at various concentrations of H_3PO_4. In RRDE experiments, the ring potential was set to 1.2 V. Before experiments, the Pt catalyst in the ring was activated by potential cycling in 0.1 M $HClO_4$ from 0 to 1.4 V at a scan rate of 50 mV s^{-1} for 10 min. The catalyst selectivity for four-electron reduction of O_2 was calculated from the H_2O_2 yield using the following equation:[15]

$$H_2O_2\ (\%) = 200 \times \frac{I_R/N}{(I_R/N) + I_D} \tag{1}$$

Here, I_D and I_R are the disk current and ring current, respectively, and N is the ring collection efficiency (36% in this work).

2.3. Physical Characterization. The surface area of catalysts was measured by nitrogen adsorption at 77 K using Brunauer−Emmett−Teller (BET) analysis on a Quantachrome Autosorb iQ-c instrument. Each sample was degassed by heating at 150 °C under vacuum prior to measuring the surface area. The metal content in Fe-based catalysts was determined by thermogravimetric analysis (TGA) using a TA Q50 instrument under flowing dry air. Raman spectra were obtained using a Kaiser Holospec Raman system at 514 nm excitation. The sample morphology was characterized by scanning electron microscopy (SEM) on a Hitachi S-5400. The crystallinity of samples was determined by X-ray diffraction (XRD) performed on an automated Rigaku diffractometer equipped with a Cu Kα radiation source and a graphite monochromator operating at 45 kV and 40 mA. The diffraction patterns were acquired at a scan rate of 1.2° min^{-1} with a step of 0.02°.

X-ray photoelectron spectrometry (XPS) was performed on an ESCA 210 and MICROLAB 310D spectrometer. The high-resolution spectra were acquired in normal emission geometry with a conventional Mg X-ray source at a pass energy of 20 eV. Transmission electron microscopy (TEM) and SEM images from the same particles were acquired using a Hitachi HF3300 TEM operated at an accelerating voltage of 300 kV. Atomically resolved aberration-corrected annular dark-field (ADF) scanning transmission electron microscopy (STEM) images were recorded using a Nion UltraSTEM-100 operated at 60 kV. Specimens were mounted on lacey carbon films using a standard drop-cast method. For inductively coupled plasma-optical emission spectroscopy (ICP-OES) analysis, the carbon component was first removed by dry-ashing the catalysts in air at 700 °C. The ash residue was then digested in a heated mixture of trace-metal-grade concentrated hydrochloric and nitric acids, and the resultant solution was diluted with water. The iron concentrations in the product solutions were measured using a PerkinElmer Optima 3300 DV ICP-OES to calculate the mass fraction of iron in the powder samples.

3. RESULTS AND DISCUSSION

3.1. ORR Activity in the Presence of H_3PO_4. It has been demonstrated before that the ORR activity of NPMCs strongly depends on the transition metal used in the synthesis.[24] In this work, iron and cobalt salts were selected as precursors for PANI-Fe-C and PANI-Co-C catalysts, respectively. NPMCs studied in this work were heat-treated at 900 °C, the temperature that provided the highest ORR activity and four-electron selectivity.[24,27] The steady-state ORR polarization and H_2O_2-yield plots, obtained with three different NPMCs in 5.0 M H_3PO_4 at a disk rotation rate of 900 rpm, are shown in Figure 1a. The reason for the use of a high concentration of
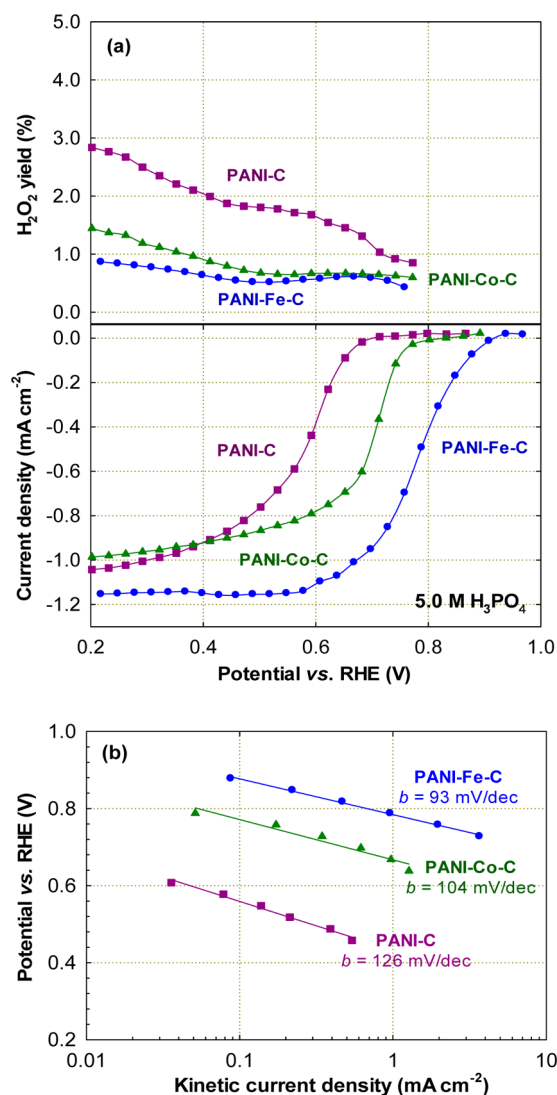

Figure 1. Effect of the metal on (a) ORR activity (bottom), H_2O_2 yield (top), and (b) Tafel plots in 5.0 M H_3PO_4 at room temperature and disk rotation rate of 900 rpm.

H_3PO_4 (5.0 M) in electrochemical testing was to mimic in the best possible way the environment of PBI membrane-based phosphoric acid fuel cells.

Of the three tested NPMCs, PANI-Fe-C gave the most positive ORR onset potential (0.92 V vs RHE) and half-wave potential (0.77 V vs RHE). The latter ORR half-wave potential value is by ca. 40 mV lower than that measured previously in 0.5 M H_2SO_4 (0.81 V).[27] The metal-free PANI-C catalyst

showed relatively poor ORR activity, attesting to the key role of the transition metal in inducing ORR activity of NPMCs. These results are in good agreement with our previous data obtained in sulfuric acid electrolyte.[17] The four-electron selectivity was found to correlate well with the ORR activity of the catalysts. The lowest H_2O_2 yield, below 1% at all studied potentials, was obtained for the PANI-Fe-C catalyst. The H_2O_2 yield of PANI-C was ca. 2%. Low H_2O_2 yields in the presence of H_3PO_4 corroborated high selectivity of the catalysts for the four-electron reduction of O_2 to H_2O rather than the two-electron reduction to H_2O_2.

The kinetic current density, extracted from the Koutecky–Levich plots, was used to generate Tafel plots in Figure 1b. Theoretically, a Tafel slope (b) of 120 mV dec^{-1} is due to the rate-determining step associated with the first electron transfer. A Tafel slope of 60 mV dec^{-1} has been linked to the effect of surface oxides or adsorbed oxygen intermediates on ORR kinetics, governed by the Temkin adsorption isotherm, according to which the activation energy of an electrochemical process becomes dependent on the surface concentration of intermediates at high surface coverage values.[28] The Tafel slope values measured with the PANI-Co-C ($b = 104$ mV dec^{-1}) and metal-free catalyst ($b = 126$ mV dec^{-1}) are close to 120 mV dec^{-1}, suggesting that the first electron transfer may be rate determining. The lower Tafel slope observed with PANI-Fe-C ($b = 93$ mV dec^{-1}) points to the possible effect of surface diffusion of the ORR intermediates.[28] It is worth noting that the Tafel slope values measured with PANI-Fe-C in 5.0 M H_3PO_4 and 0.5 M H_2SO_4 are very similar, 93 and 87 mV/dec, respectively, suggesting a very similar or the same ORR reaction mechanism in both electrolytes. Since the Tafel slope and onset potential values for PANI-Fe-C and PANI-Co-C catalysts are different, the ORR reaction mechanism and active sites are likely different, too.[29,30] This is supported by the large difference in the onset ORR potentials for the two catalysts by as much as 90 mV (Figure 1a).

The ORR activity and four-electron selectivity of the PANI-Fe-C catalyst in 5.0 M phosphoric acid were also studied as a function of initial Fe loadings between 3 and 30 wt % (Figure 2a). A significant improvement in the ORR was found with a catalyst synthesized using 10 wt % of Fe, relative to the catalyst obtained using 3 wt % of Fe. An increase in the ORR current was observed in the mass-transfer region and, however small, in the kinetic region when the Fe content in the synthesis was raised to 30 wt %. PANI-Fe-C synthesized using 30 wt % of Fe generated the least amount of H_2O_2 — below 1% — a very low value for a nonprecious metal ORR catalyst. The observed ORR activity correlated well with the BET surface area of the PANI-Fe-C catalysts. The electrochemical surface area (S_a) values for three PANI-Fe-C samples (Figure 2b) were calculated from the double layer capacitance determined by cyclic voltammetry,[31–34] using 0.2 F m^{-2} (20 μF cm^{-2}) as the "unit" capacitance of carbon-based catalysts. This is the value used before for glassy carbon.[35] While this approach is not exact it represents a good S_a estimate.

In the same trend as BET surface area data, the 30 wt % Fe-derived catalyst reveals the highest electrochemical surface area of 235 m^2 g^{-1}, compared to 97 m^2 g^{-1} and 59 m^2 g^{-1}, measured with 10 and 3 wt % Fe samples, respectively. It is worth noting that the BET surface area, measured by N_2 adsorption from a gas phase, includes the area of micropores (<2.0 nm). In turn, S_a, the effective electrochemical surface area, represents only that fraction of the BET area that is accessible to the electrolyte.
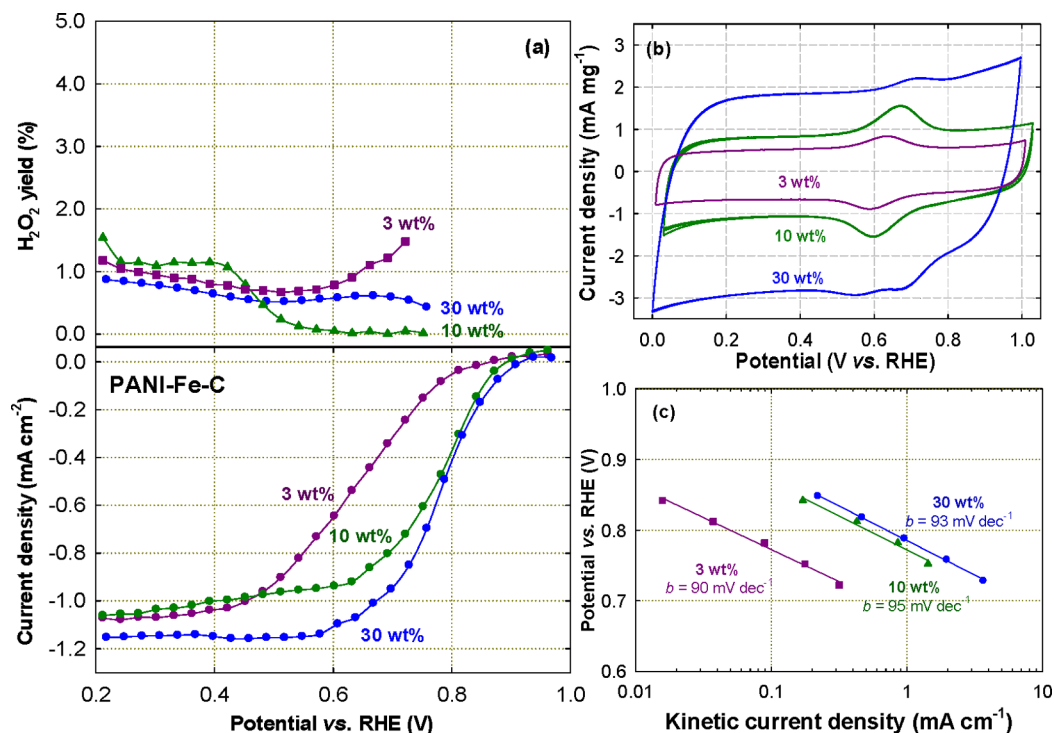
Figure 2. Impact of Fe loading on (a) ORR activity (bottom), H_2O_2 yield (top), (b) cyclic voltammograms in 0.5 M H_2SO_4 at 25 °C and a scan rate of 50 mV s^{-1} for various PANI-Fe-C catalysts used to calculate the electrochemically accessible surface areas, and (c) Tafel plots in 5.0 M H_3PO_4 at room temperature and disk rotation rate of 900 rpm. Fe loadings is the initial weight percentages of Fe during the synthesis.

S_a is predominantly associated with mesopores (>2 nm) and macropores (>50 nm).[36,37] This is the reason why S_a for high surface-area catalysts is always smaller than the BET surface area. At the same time, the reaction mechanism was found to be independent of the Fe content, as suggested by similar Tafel slope values, which were all in the range from 90 to 97 mV dec^{-1} (Figure 2c).

The number of electrons involved in the ORR at different potentials using the best performing 30 wt % Fe-derived PANI-Fe-C catalyst was calculated from the Koutecky–Levich plots (Figure 3). As shown in Figure 3b, the Koutecky–Levich plots at 0.49 and 0.37 V overlap and are also parallel to the plots recorded at 0.61 and 0.70 V, indicating that the number of electrons transferred in the ORR remains constant in the studied potential range. The n values of 3.63–3.93 (with a mean value of 3.78), calculated from the slope of the Koutecky–Levich plots in Figure 3b, are slightly lower than the n values of 3.98–3.99 obtained from RRDE data in Figure 2a. This difference likely results from the high sensitivity of the slope and intercept values of the Koutecky–Levich lines to any scatter in the experimental data. The high values of n attest to either a direct four-electron or a two-plus-two-electron mechanism of oxygen reduction on the studied NPMCs in concentrated H_3PO_4.

3.2. Catalyst Morphology. To learn more about the origin of ORR activity of PANI-Fe-C catalysts, the physical and chemical properties the catalysts were studied as a function of Fe loading used in the synthesis. The bulk Fe content and BET surface area of three PANI-Fe-C catalysts are shown in Table 1. While, surprisingly, the Fe content in the catalyst synthesized using 30 wt % Fe is the lowest (~2 wt %), the BET surface area of that catalyst is the highest, 845 m^2 g^{-1} (a high value for a KJ-supported NPMC).[24] Noteworthy, while the nominal metal content of Co used for synthesizing the PANI-Co-C catalyst
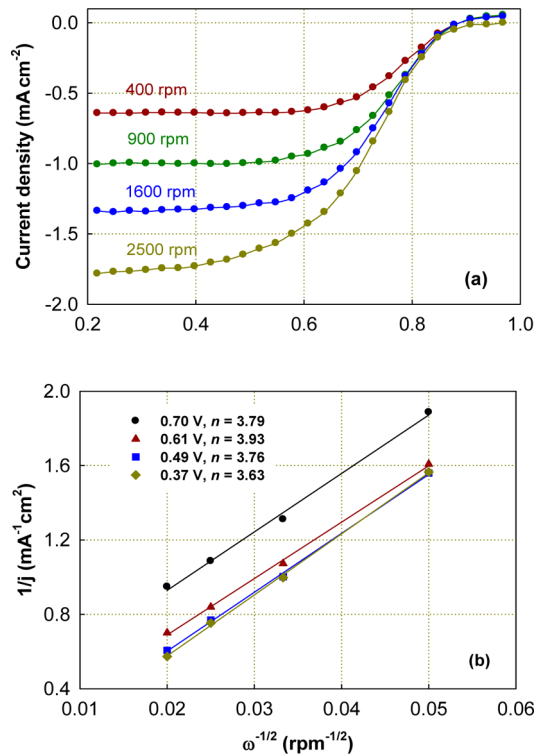

Figure 3. (a) Steady-state ORR polarization plots recorded with the 30 wt % Fe-derived PANI-Fe-C catalyst in an oxygen-saturated 5.0 M H_3PO_4 solution at various disk rotation rates; (b) corresponding Koutecky–Levich plots.

was 30 wt % the Co content in the final catalyst was 8 wt %. In good agreement with the BET surface-area values, SEM images in Figure 4 attest to a significantly more porous structure for

Table 1. Fe Content and BET Surface Area of PANI-Fe-C Catalysts

Fe loading in synthesis (nominal, wt %)	Fe content in final catalysts (by ICP and TGA, wt %)	BET surface area (m²/g)
3%	10%	148
10%	12%	292
30%	2%	845

the 30 wt % Fe-derived catalyst than for the 3 and 10 wt % Fe-derived catalysts.

The distinct XRD peaks in Figure 4 (shown by red star) for 3 and 10 wt % Fe-derived catalysts can be assigned to FeS (2θ = 17.1°, 18.7°, 29.9°, 31.9°, 33.7°, 35.7°, 43.3°, 47.2°, 54.0°, 63.5°, and 70.8°).[38] The sulfide originates from the use of APS as oxidant for aniline polymerization during the catalyst synthesis (see Experimental Section for details). Of note is the lack of FeS peaks in the XRD spectrum from the 30 wt % Fe-derived catalyst, which only contains carbon peaks at ca. 25° and 44°.[39] In contrast to the 3 and 10 wt % Fe-derived catalysts, *in situ* formed FeS in the 30 wt % Fe-derived catalyst is more efficiently leached out during the acid treatment step. The fact that the highest initial Fe loading used in the synthesis leads to the lowest bulk Fe content in the final product as well as the highest BET surface area may indicate that the *in situ* formed FeS acts as an effective sacrificial pore-forming agent during acid leaching. It is possible that the FeS particles formed with lower Fe loadings of 3 and 10 wt % are more fully encapsulated within carbon agglomerates (Figure 4), protecting them during the acid leaching.[40] More research is required to understand why the FeS formed with 30 wt % of Fe is not protected by carbon layers.

Advanced TEM and STEM were performed to study the 30 wt % Fe PANI-Fe-C catalyst to provide additional insight regarding the structure of the newly developed catalysts with high surface area. As shown in Figure 5a, the predominant morphology consisted of an intimate mixture of agglomerated KJ particles and rumpled, multilayered graphene sheets. Fe

particles, most likely FeS, were also occasionally identified (yellow arrow, Figure 5a). An SEM image (Figure 5b) of the same region shown in the TEM image in Figure 5a also indicates that the rumpled, sheet-like morphology of the multilayered graphene envelopes the KJ particles. In Figure 5c, an ADF-STEM image of a multilayered graphene sheet and associated EELS analysis indicates that single Fe atoms are dispersed across the surface of the graphene. These Fe atoms were highly mobile under the electron beam, indicating that Fe is not incorporated within the carbon lattice. Additionally, EELS identified nitrogen in thicker areas of the layered graphene sheets.

At this point, one can only speculate on the unique graphene morphology of the carbon observed in 30 wt % Fe-derived catalysts. Larger FeS nanoparticles in 3 and 10 wt % Fe-derived catalysts appear to be locked within agglomerated carbon particles, while smaller FeS particles in the 30 wt % Fe-derived catalyst are enveloped in thin sheets of graphene and thus exposed. The carbon morphology in 3 and 10 wt % Fe-derived catalysts is clearly more agglomerated and sphere-like, rather than layer- or sheet-like. The formation of graphene sheets is a direct result of the initial higher Fe-content; the fact that most of it disappears during acid leaching is also a direct result of the formation of the graphene sheets. The XPS analysis of the three PANI-Fe-C catalysts supports the hypothesis of the FeS leaching by revealing that Fe and S content near the catalyst surface decreases with an increase in the Fe loading used in the synthesis (Table 2). It is worth noting that a decrease in the total nitrogen content is observed with an increase in the amount of Fe precursor without an associated drop in ORR activity. This suggests that ORR activity of these NPMCs does not depend on the total nitrogen doping but, more likely, on the location and bonding of the nitrogen atoms within the carbon/graphene lattice.[41−43] Relative to the two catalysts with lower initial Fe loadings, the high-resolution N 1s peak for the 30 wt % Fe-derived catalyst shows that the relative amount of graphitic nitrogen increases with the Fe loading,[12] leading to an
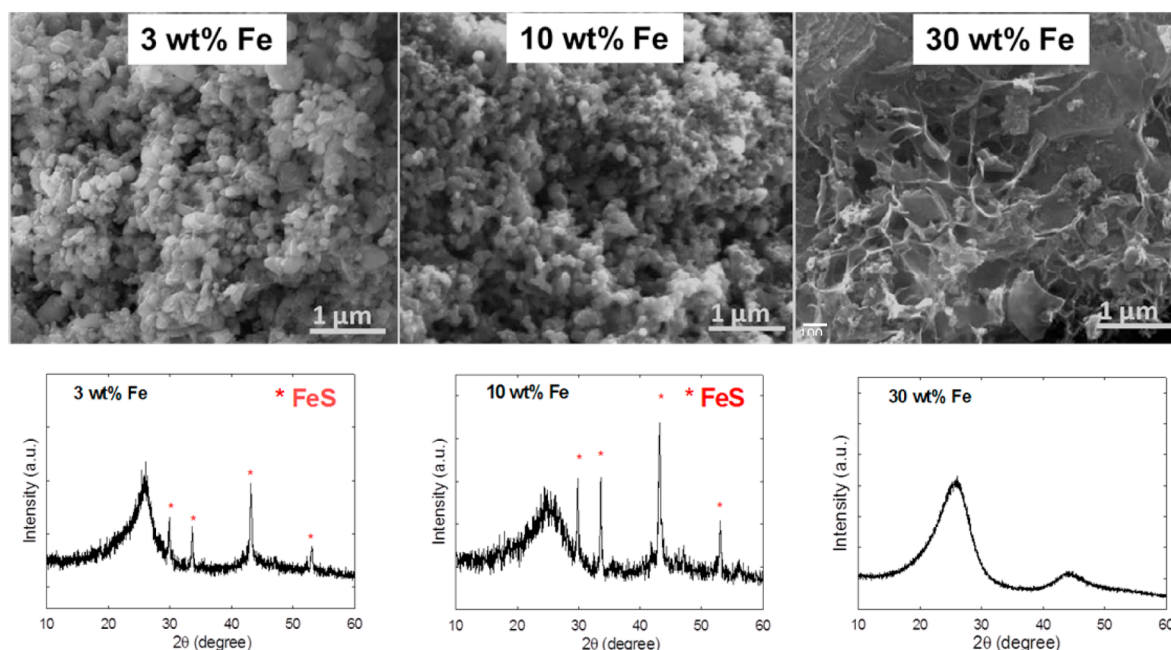

Figure 4. SEM images (top) and XRD patterns (bottom) for PANI-Fe-C catalysts as a function of Fe loading used during the synthesis.
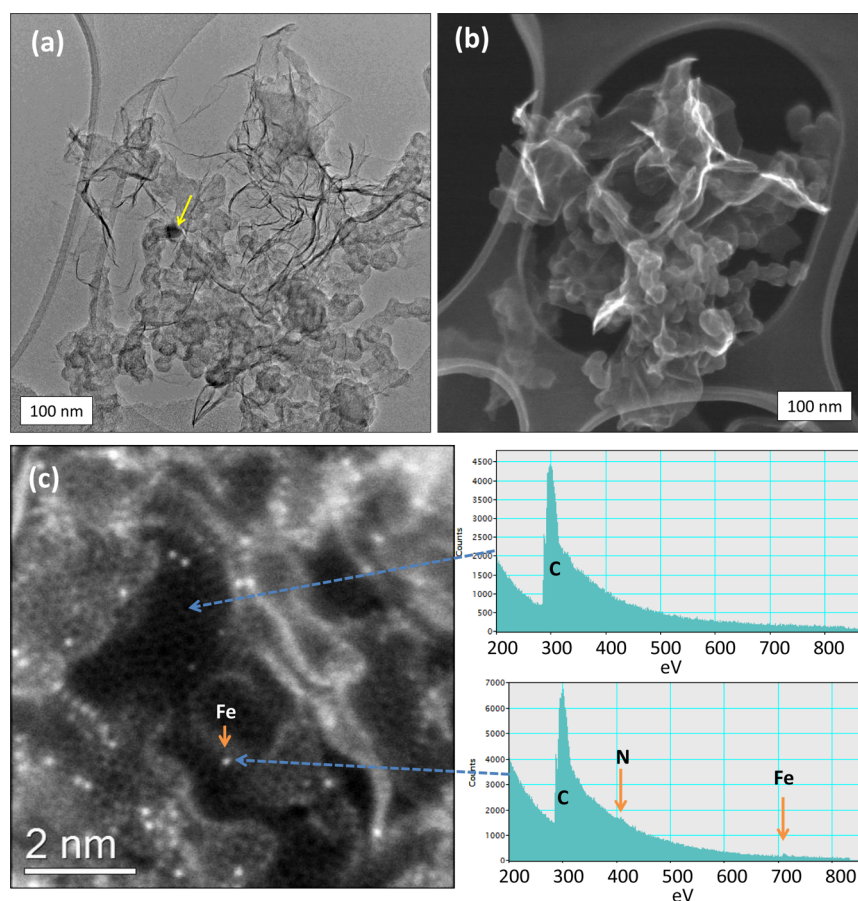
Figure 5. Microscopy analysis of 30 wt % Fe-derived PANI-Fe-C catalysts. (a) TEM image and (b) SEM image of the same agglomerated area showing KJ particles mixed with multilayered graphene sheets. The yellow arrow indicates a large FeS particle. (c) ADF-STEM of graphene sheet and associated EEL spectra showing the presence of single Fe atoms on the surface of graphene.

Table 2. Elemental Analysis of PANI-Fe-C Catalysts

Fe loading in synthesis, wt %	atomic content, %				
	S	N	C	Fe	O
3%	1.18	6.62	87.24	0.68	4.29
10%	0.63	4.59	89.85	0.48	4.51
30%	0.25	3.61	89.67	0.26	6.21

enhancement in the ORR activity in H_3PO_4 and implying that graphitic nitrogen can significantly impact catalyst activity.

3.3. ORR Performance of NPMCs vs Pt/C Catalysts. The effect of H_3PO_4 on the ORR activity of the 30 wt % Fe-derived catalyst compared with a Pt/C reference catalyst was studied in O_2-saturated 0.1 M $HClO_4$ solution as a function of H_3PO_4 concentration (Figure 6). The ORR activity of the 30 wt % Fe-derived catalyst is nearly independent of H_3PO_4 concentration (Figure 6a), as is the double layer capacitance in N_2-saturated 0.1 M $HClO_4$ solution (Figure 6b). A gradual drop in the limiting current in the electrolyte with increasing H_3PO_4 concentration (Figure 6a) is caused by lower values of the diffusion coefficient and O_2 solubility as well as a higher value of the kinematic viscosity of H_3PO_4 relative to 0.1 M $HClO_4$ solution (effectively water). They all lead to a decrease in the mass-transfer-limited current of oxygen oxidation.[44] These results are very different from those obtained with a Pt/C reference catalyst, which exhibit a loss in the ORR activity by as much as ca. 60 mV at $E_{1/2}$ in 0.3 M H_3PO_4 (Figure 6c). Cyclic voltammetry (Figure 6d) indicates that the number of Pt sites

for hydrogen adsorption decreases with an increase in phosphoric acid concentration as a result of phosphate adsorption, an observation that is in good agreement with previous results.[45] The potential of Pt-surface oxidation shifts positively in the presence of phosphates, confirming the formation of a strong chemical bond between the phosphate ions and Pt atoms.

ORR polarization plots recorded with the 30 wt % Fe-derived catalyst and the reference Pt/C catalyst at two Pt loadings of 20 μg_{Pt} cm^{-2} and 60 μg_{Pt} cm^{-2} in 5.0 M H_3PO_4 are shown in Figure 7. The NPMC performance trails that of the Pt/C reference catalyst, but only when the high Pt loading of 60 μg_{Pt} cm^{-2} is used. The NPMC clearly outperforms the Pt/C reference at a "standard" RDE loading of 20 μg_{Pt} cm^{-2}, often viewed as representative for fuel cell cathode applications. The higher value of limiting current density for the NPMC has been linked to the greater thickness of the NPMC layer.[2,25,46] It should be pointed out that all electrochemical measurements in this work were carried out at a room temperature. The experiments focusing on the effect of temperature on performance of a fuel cell with a PBI-type membrane at 150 °C, and possibly at higher temperatures, are planned. We hope to report results of this study in the near future, together with the data on the optimization of the NPMC cathode.

4. CONCLUSIONS

The ORR activity of Pt/C is significantly reduced in H_3PO_4-based electrolytes due to severe poisoning of the catalyst
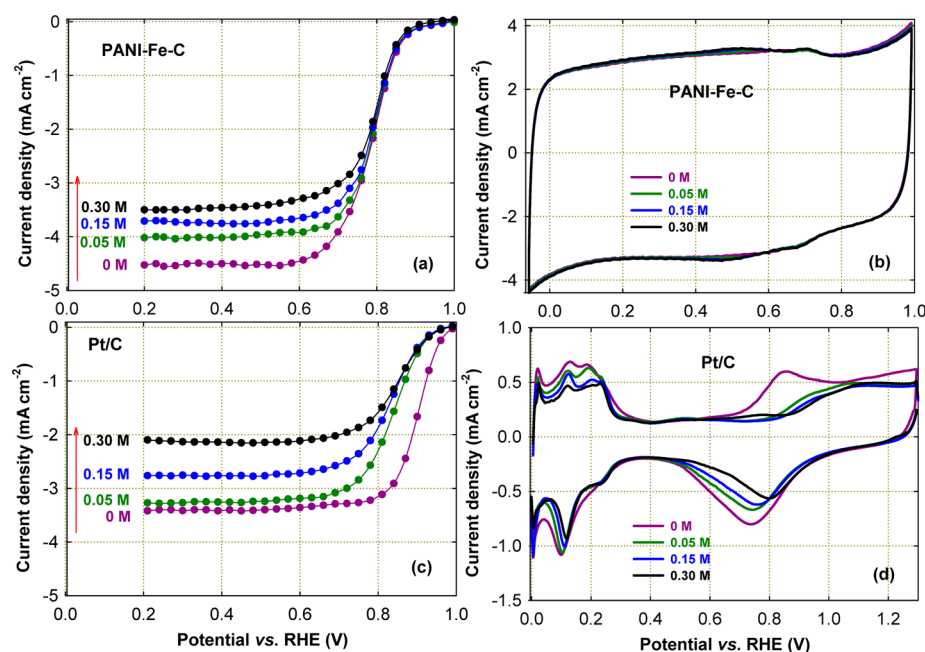
Figure 6. (a, c) Steady-state ORR polarization plots and (b, d) cyclic voltammograms recorded with 30 wt % Fe-derived catalyst (top) and 60 μg_{Pt} cm^{-2} Pt/C (bottom) in O$_2$- and N$_2$-saturated 0.1 M HClO$_4$ electrolyte as a function of H$_3$PO$_4$ concentration. Rotation rate: 900 rpm; CV scan rate 10 mV/s; room temperature.

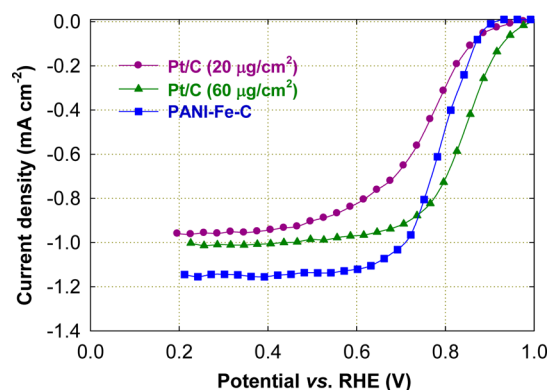**Figure 7.** ORR activity comparison between 30 wt % Fe-derived nonprecious metal catalyst, 20 μg_{Pt} cm^{-2} and 60 μg_{Pt} cm^{-2} Pt/C catalysts in O$_2$-saturated 5.0 M H$_3$PO$_4$ electrolyte by steady-state polarization curves. Rotation rate: 900 rpm; room temperature.

surface by chemisorbed H$_2$PO$_4^-$ and HPO$_4^{2-}$ ions. In this study, PANI-Fe-C catalysts for oxygen reduction, derived from polyaniline, transition metal, and carbon, were studied in phosphoric acid electrolytes. These NMPCs showed much improved phosphate tolerance compared to their Pt/C counterparts. The use of a high Fe loading in the PANI-Fe-C catalyst synthesis (30 wt %) resulted in a final catalyst with an extremely low Fe content but high surface area (845 m^2 g^{-1}) and enhanced ORR activity, likely due to the formation of a unique carbon morphology (sheet-like multilayered graphene), which also results in improved acid leaching of the FeS. Although the catalyst obtained using the higher Fe loading has relatively low nitrogen content, its activity is higher than that of the two other Fe-based catalysts, indicating that ORR performance of NPMCs depends more on how nitrogen is incorporated into the carbon/graphene lattice rather than on the total nitrogen content. RRDE experiments and kinetic analysis attest to a four-electron selectivity of nonprecious

metal ORR catalysts in H$_3$PO$_4$ electrolytes. Further understanding of the factors governing the ORR activity of nonprecious metal catalysts in the presence of phosphates as well as their implementation into a PBI-based HT-PEFCs will be the focus of our future research.

■ AUTHOR INFORMATION

Corresponding Authors
*E-mail: wugang@lanl.gov (G.W.).
*E-mail: zelenay@lanl.gov (P.Z.).
Notes
The authors declare no competing financial interest.

■ ACKNOWLEDGMENTS

■ REFERENCES

(1) Cao, Y. C.; Wang, X.; Mamlouk, M.; Scott, K. *J. Mater. Chem.* **2011**, *21*, 12910−12916.
(2) Carrette, L.; Friedrich, K. A.; Stimming, U. *Fuel Cells* **2001**, *1*, 5−39.
(3) Li, Q. F.; Hjuler, H. A.; Bjerrum, N. J. *J. Appl. Electrochem.* **2001**, *31*, 773−779.
(4) Asensio, J. A.; Sanchez, E. M.; Gomez-Romero, P. *Chem. Soc. Rev.* **2010**, *39*, 3210−3239.
(5) Quartarone, E.; Mustarelli, P. *Energy Environ. Sci.* **2012**, *5*, 6436−6444.
(6) Kongstein, O. E.; Berning, T.; Borresen, B.; Seland, F.; Tunold, R. *Energy* **2007**, *32*, 418−422.
(7) Pinar, F. J.; Canizares, P.; Rodrigo, M. A.; Ubeda, D.; Lobato, J. *J. Power Sources* **2011**, *196*, 4306−4313.
(8) He, Q. G.; Yang, X. F.; Chen, W.; Mukerjee, S.; Koel, B.; Chen, S. W. *Phys. Chem. Chem. Phys.* **2010**, *12*, 12544−12555.

(9) Lee, K. S.; Yoo, S. J.; Ahn, D.; Kim, S. K.; Hwang, S. J.; Sung, Y. E.; Kim, H. J.; Cho, E.; Henkensmeier, D.; Lim, T. H.; Jang, J. H. *Electrochim. Acta* **2011**, *56*, 8802−8810.

(10) Kamat, A.; Herrmann, M.; Ternes, D.; Klein, O.; Krewer, U.; Scholl, S. *Fuel Cells* **2011**, *11*, 511−517.

(11) He, Q. G.; Li, Q.; Khene, S.; Ren, X. M.; López-Suárez, F. E.; Lozano-Castelló, D.; Bueno-López, A.; Wu, G. *J. Phys. Chem. C* **2013**, *117*, 8697−8707.

(12) Wu, G.; Zelenay, P. *Acc. Chem. Res.* **2013**, *46*, 1878−1889.

(13) Jaouen, F.; Proietti, E.; Lefevre, M.; Chenitz, R.; Dodelet, J.-P.; Wu, G.; Chung, H. T.; Johnston, C. M.; Zelenay, P. *Energy Environ. Sci.* **2011**, *4*, 114−130.

(14) Wu, G.; Cui, G.; Li, D.; Shen, P.-K.; Li, N. *J. Mater. Chem.* **2009**, *19*, 6581−6589.

(15) Nallathambi, V.; Lee, J.-W.; Kumaraguru, S. P.; Wu, G.; Popov, B. N. *J. Power Sources* **2008**, *183*, 34−42.

(16) Lefèvre, M.; Proietti, E.; Jaouen, F.; Dodelet, J.-P. *Science* **2009**, *324*, 71−74.

(17) Wu, G.; Chung, H. T.; Nelson, M.; Artyushkova, K.; More, K. L.; Johnston, C. M.; Zelenay, P. *ECS Trans.* **2011**, *41*, 1709−1717.

(18) Chung, H. T.; Johnston, C. M.; Artyushkova, K.; Ferrandon, M.; Myers, D. J.; Zelenay, P. *Electrochem. Commun.* **2010**, *12*, 1792−1795.

(19) Li, Q.; Xu, P.; Gao, W.; Ma, S. G.; Zhang, G. Q.; Cao, R. G.; Cho, J.; Wang, H. L.; Wu, G. *Adv. Mater.* **2014**, *26*, 1378−1386.

(20) Wu, G.; Nelson, M.; Ma, S.; Meng, H.; Cui, G.; Shen, P. K. *Carbon* **2011**, *49*, 3972−3982.

(21) Wu, G.; More, K. L.; Xu, P.; Wang, H. L.; Ferrandon, M.; Kropf, A. J.; Myers, D. J.; Ma, S. G.; Johnston, C. M.; Zelenay, P. *Chem. Commun.* **2013**, *49*, 3291−3293.

(22) Wu, G.; Artyushkova, K.; Ferrandon, M.; Kropf, J.; Myers, D.; Zelenay, P. *ECS Trans.* **2009**, *25*, 1299−1311.

(23) Maass, S.; Finsterwalder, F.; Frank, G.; Hartmann, R.; Merten, C. *J. Power Sources* **2008**, *176*, 444−451.

(24) Wu, G.; Johnston, C. M.; Mack, N. H.; Artyushkova, K.; Ferrandon, M.; Nelson, M.; Lezama-Pacheco, J. S.; Conradson, S. D.; More, K. L.; Myers, D. J.; Zelenay, P. *J. Mater. Chem.* **2011**, *21*, 11392−11405.

(25) Wu, G.; Nelson, M. A.; Mack, N. H.; Ma, S. G.; Sekhar, P.; Garzon, F. H.; Zelenay, P. *Chem. Commun.* **2010**, *46*, 7489−7491.

(26) Wu, G.; More, K. L.; Johnston, C. M.; Zelenay, P. *Science* **2011**, *332*, 443−447.

(27) Ferrandon, M.; Wang, X.; Kropf, A. J.; Myers, D. J.; Wu, G.; Johnston, C. M.; Zelenay, P. *Electrochim. Acta* **2013**, *110*, 282−291.

(28) Coutanceau, C.; Croissant, M. J.; Napporn, T.; Lamy, C. *Electrochim. Acta* **2000**, *46*, 579−588.

(29) Wu, G.; Mack, N. H.; Gao, W.; Ma, S. G.; Zhong, R. Q.; Han, J. T.; Baldwin, J. K.; Zelenay, P. *ACS Nano* **2012**, *6*, 9764−9776.

(30) Holby, E. F.; Wu, G.; Zelenay, P.; Taylor, C. D. *J. Phys. Chem. C* **2014**, *118*, 14388−14393.

(31) Wu, G.; Chen, Y.-S.; Xu, B.-Q. *Electrochem. Commun.* **2005**, *7*, 1237−1243.

(32) Wu, G.; Swaidan, R.; Li, D.; Li, N. *Electrochim. Acta* **2008**, *53*, 7622−7629.

(33) Wu, G.; Xu, B.-Q. *J. Power Sources* **2007**, *174*, 148−158.

(34) Wu, G.; Li, L.; Li, J.-H.; Xu, B.-Q. *Carbon* **2005**, *43*, 2579−2587.

(35) Zhou, Y.-K.; He, B.-L.; Zhou, W.-J.; Huang, J.; Li, X.-H.; Wu, B.; Li, H.-I. *Electrochim. Acta* **2004**, *49*, 257−262.

(36) Rolison, D. R. *Science* **2003**, *299*, 1698−1701.

(37) Shi, H. *Electrochim. Acta* **1996**, *41*, 1633−1639.

(38) King, H. E.; Prewitt, C. T. *Acta Crystallogr., Sect. B: Struct. Crystallogr. Cryst. Chem.* **1982**, *38*, 1877−1887.

(39) Shi, H.; Reimers, J. N.; Dahn, J. R. *J. Appl. Crystallogr.* **1993**, *26*, 827−836.

(40) Wu, G.; Dai, C.; Wang, D.; Li, D.; Li, N. *J. Mater. Chem.* **2010**, *20*, 3059−3068.

(41) Li, Q.; Cao, R.; Cho, J.; Wu, G. *Phys. Chem. Chem. Phys.* **2014**, *16*, 13568−13582.

(42) Li, Q.; Cao, R.; Cho, J.; Wu, G. *Adv. Energy Mater.* **2014**, *4*, 201301415.

(43) Ferrandon, M.; Kropf, A. J.; Myers, D. J.; Artyushkova, K.; Kramm, U.; Bogdanoff, P.; Wu, G.; Johnston, C. M.; Zelenay, P. *J. Phys. Chem. C* **2012**, *116*, 16001−16013.

(44) Gan, F.; Chin, D. T. *J. Appl. Electrochem.* **1993**, *23*, 452−455.

(45) Furuya, N.; Koide, S. *Surf. Sci.* **1989**, *220*, 18−28.

(46) Steiger, B.; Anson, F. C. *Inorg. Chem.* **2000**, *39*, 4579−4585.